processes

MDPI

Article

Surface-Passivated Single-Crystal Micro-Plates for Efficient Perovskite Solar Cells

Tzu-Hsueh Wu [1], Ganesh D. Sharma [2,3] and Fang-Chung Chen [1,4,*]

[1] Department of Photonics, College of Electrical and Computer Engineering, National Yang Ming Chiao Tung University, Hsinchu 30010, Taiwan; handsome27805@gmail.com
[2] Department of Physics, The LNM Institute of Information Technology, Jaipur 302031, India; gdsharma273@gmail.com
[3] Department of Electronics and Communication Engineering, The LNM Institute of Information Technology, Jaipur 302031, India
[4] Center for Emergent Functional Matter Science, National Yang Ming Chiao Tung University, Hsinchu 30010, Taiwan
* Correspondence: fcchendop@nycu.edu.tw

Abstract: Perovskite solar cells (PeSCs) prepared with single crystals (SCs) ideally exhibit higher power conversion efficiencies (PCEs) because they possess a lower density of structural imperfection and superior charge transport. However, the density of the surface defects on the SCs is still very high, thereby inevitably affecting the device performance. Herein, perovskite single-crystal micro-plates were grown on a hole-transporting material, poly[bis(4-phenyl)(2,4,6-trimethylphenyl) amine], through a space-limited inverse temperature crystallization method. The surfaces of the as-prepared SCs were passivated using trioctylphosphine oxide (TOPO) during the device fabrication to alleviate the impact of surface defects. The PCE values are averagely improved from 11.90 ± 0.30% to 14.76 ± 0.65% after the surface passivation; the champion device even exhibits a PCE of 15.65%. The results from photoluminescence and hole-only devices reveal that TOPO treatments effectively reduce the number of surface defects on the single crystals, thereby improving the photovoltaic performance. The surface passivation also inhibits the hysteresis behavior due to the lower defect density. Finally, the TOPO treatment also improves the stability of the single-crystal PeSCs, presumably due to the hydrophobic long alkyl chains. Thus, this work provides an effective approach to achieving high efficiencies of single-crystal PeSCs.

Keywords: perovskite; solar cell; single crystal; defect; surface passivation

Citation: Wu, T.-H.; Sharma, G.D.; Chen, F.-C. Surface-Passivated Single-Crystal Micro-Plates for Efficient Perovskite Solar Cells. *Processes* **2022**, *10*, 1477. https://doi.org/10.3390/pr10081477

Academic Editor: Blaž Likozar

Received: 12 July 2022
Accepted: 26 July 2022
Published: 28 July 2022

1. Introduction

Halide perovskite materials are receiving a great deal of attention because of their remarkable properties: low cost, high absorption coefficients, high defect tolerance, and solution-processability [1–3]. The power conversion efficiencies (PCEs) of perovskite solar cells (PeSCs) have approached 26%, which is comparable with those of single-crystalline Si solar cells [4]. Further, many other electronic devices fabricated with halide perovskite materials, including light-emitting devices (LEDs) [5–7], lasers [8,9], photodetectors [10,11], and radiation detectors [12,13], have shown promising performances for the next-generation applications.

Most perovskite thin films for device applications so far are polycrystalline [1]. Grain boundaries (GBs) abundantly exist in the perovskite active layers and the defects on the GBs inevitably impede charge transport, thereby limiting the efficiencies of the devices. On the other hand, perovskite single crystals (SCs) ideally would exhibit a better device performance than that of the cells prepared with polycrystalline thin films because the density of defects in the SCs is lower [14–16]. Further, perovskite SCs exhibit longer carrier diffusion lengths, allowing for thicker perovskite films to be used for device fabrication [14].

For solar applications, thicker perovskite active layers increase the absorption capability of the solar irradiation [17]. For many radiation detectors, their stopping power against ionizing radiations also increases with the thickness [12]. Therefore, perovskite SCs are very promising for the optoelectronic applications that require thick films.

Bulk perovskite SCs are easier to synthesize; however, they are not suitable for device fabrication directly. For instance, effective charge collection is required for achieving high PCEs of PeSCs, and the carrier diffusion length of perovskite SCs should be comparable or even longer than the thickness of the SCs to collect the charges effectively. Therefore, many approaches for preparing asymmetric SCs (single-crystal films) are proposed for fabricating highly efficient single-crystal PeSCs [15–29]. A cavitation-triggered asymmetric method, for example, is reported for growing perovskite monocrystalline films, and the single-crystal solar cells achieved a PCE of 6.53% [18]. More recently. a low-temperature crystallization method for growing thin single-crystal films was also designed via solvent engineering; a high PCE of 21.9% was achieved [16]. Alsalloum et al. incorporate a mixed-cation single-crystal layer ($FA_{0.6}MA_{0.4}PbI_3$) and demonstrate that the near-infrared response of the devices can be expanded beyond those of polycrystalline $FAPbI_3$ by approximately 50 meV, yielding PCEs of up to 22.8% [19]. Two-dimensional asymmetrical SCs, which exhibit a higher air stability, were also prepared, and a PCE higher than 16% was achieved [26].

Nevertheless, the PCEs of single-crystal PeSCs are still behind those of devices prepared with polycrystalline active layers. One of the major problems for single-crystal PeSCs is the presence of surface defects. While the bulk trap density of single crystals should be very limited, the density of surface defects could still be very high [17]. Although the surface passivation effect on single-crystal PeSCs has been investigated in previous literatures [17], systematical studies are still very rare. Herein, perovskite single-crystal micro-plates were grown on a hole-transporting material, poly[bis(4-phenyl)(2,4,6-trimethylphenyl)amine] (PTAA), through a space-limited inverse temperature crystallization method. The surfaces of the SCs were passivated by using trioctylphosphine oxide (TOPO) during the device fabrication to alleviate the impact of surface defects. The PCE is averagely improved from 11.90 $\pm$ 0.30% to 14.76 $\pm$ 0.65% after the surface passivation; the champion device even exhibits a PCE of 15.65%. Our results indicate that the surface defects affect the performance of the single-crystal PeSCs significantly, and the approach we report herein can effectively improve the PCEs of single-crystal PeSCs.

2. Materials and Methods

2.1. Crystal Growth and Device Fabrication

The single-crystal micro-plates were synthesized following the crystallization method, differential space-limited crystallization (DSLC), that we have reported previously [25]. Figure 1 displays the DSLC method and the procedures for fabrication of the single-crystal solar cells. The details of the fabrication procedures can also be found in our previous reports [24–26]. In short, a layer of PTAA was spin-coated from a mixture solution consisting of N,N-dimethylformamide (DMF) and chlorobenzene (CB) (DMF:CB = 1:2, v/v) on the indium tin oxide (ITO)-coated glass substrates to modify the surface properties of the confined space [24,30]; 4-isopropyl-4′-methyldiphenyliodonium tetrakis(pentafluorophenyl)borate (TPFB, 15 wt%) was added into the PTAA solutions to reduce the resistance of the interlayer [24]. The PTAA films were further annealed at 100 °C for 10 min. The PTAA also served as the hole transport layer (HTL) of the PeSCs. As shown in Figure 1, two types of polytetrafluoroethylene (PTFE) tapes were used as spacers to control the thickness of the SCs; the first tape (thickness: 50 μm) controlled the gap between the two substrates and the second (thickness: 40 μm) was placed on the surface of the glass substrate, leaving a space of 10 μm for crystal growth. A precursor solution of CH_3NH_3I (MAI), formamidinium iodide (FAI) and PbI_2 with a molar ratio of 0.75:0.25:1 was prepared in γ-butyrolactone (GBL). The substrate was preheated to 90 °C before the loading of the precursor solution. After the injection of the precursor solution into the space between the two glass substrates, the temperature was increased to 115 °C for 30 min and was then slowly increased to

165 °C with a rate of approximately 10 °C h^{-1}. After heating for approximately 12 h in total, we could observe several $MA_{0.75}FA_{0.25}PbI_3$ SCs that appeared inside the space. The SCs were carefully wiped dry with filter paper and further cleaned/washed with isopropanol (IPA). The SCs on the PTAA/ITO substrates were annealed at 100 °C for 5 min and were transferred to a N_2-filled glove box. Then, a solution of TOPO in CB was spin-coated (3500 rmp, 60 s) on the SCs. The sample was dried under normal flow condition inside the glove box without any heating for 10 min. Then, a solution of [6,6]-phenyl-C_{61}-butyric acid methyl ester ($PC_{61}BM$, 2.3 wt%) in CB was spin-coated onto the SCs to serve as the electron transporting layer. Finally, 80 nm Cu was thermally deposited as the cathode. The device area, defined by a shadow mask, was 0.01 cm^2.

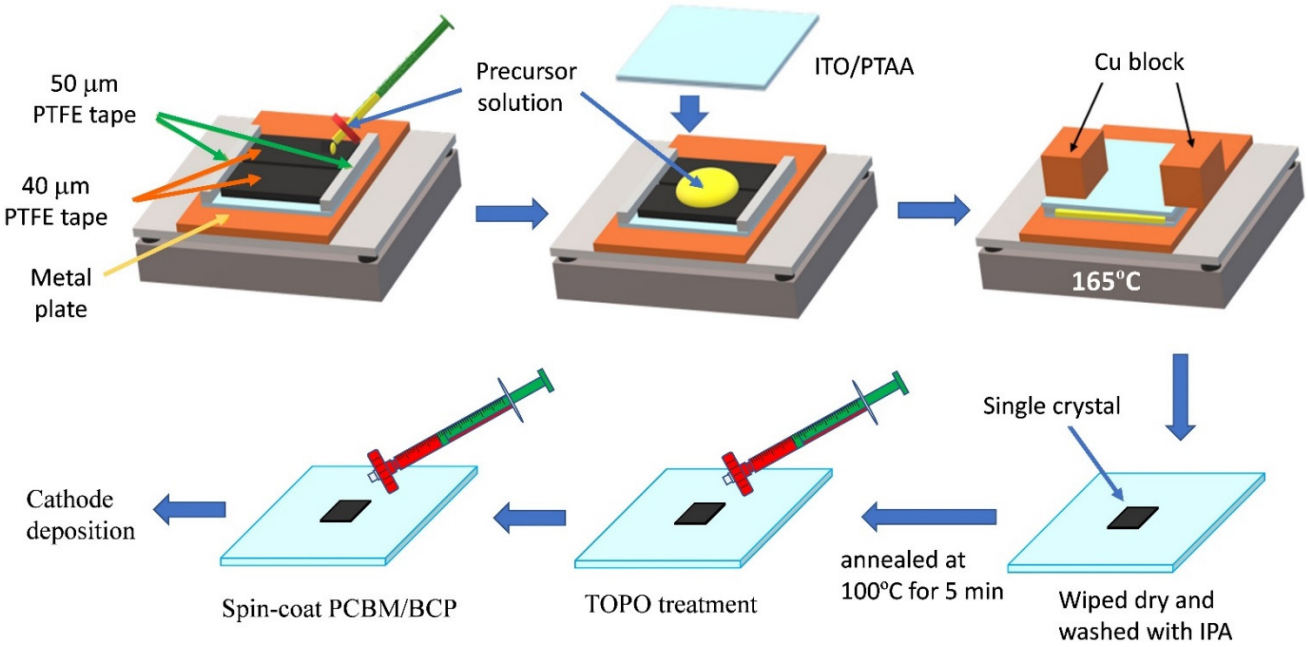

Figure 1. The procedures for the synthesis of the perovskite single-crystal micro-plates and the fabrication of the single-crystal solar cells.

2.2. Device Measurements and Characterization

The solar cells prepared using perovskite SCs were directly characterized in air without encapsulation. A test clip and a needle probe were used to connect the electrodes of the PeSCs; the details of the measurement setup can be found in the previous report [26]. The solar cells were illuminated from a standard AM1.5G solar simulator (100 mW cm^{-2}); the light intensity of the solar simulator was calibrated using a Hamamatsu Si photodiode equipped with a KG-5 filter. The photocurrent–voltage (*J*–*V*) curves were obtained using a Keithley 2400 source measure unit. The corresponding external quantum efficiency (EQE) spectra were measured using an Enli system. Time-resolved photoluminescence (TRPL) spectra were recorded using a micro-PL system, comprising a 375 nm pulse laser (PDL 200-B; PicoQuant Gmb), a HORIBA monochromator (iRH-550), and a time-correlated single photon counting system (TimeHarp).

3. Results

Figure 2a displays the device structure of the single-crystal PeSCs. The SCs were grown on TPFB-doped PTAA interlayers. $PC_{61}BM$ was deposited on the SCs and served as the electron transport layer. A layer of Cu was deposited as the cathode. Figure 2b shows a typical scanning electron microscopy (SEM) image of the SCs. The side-view image clearly indicated that the thickness of the SC was 9.7 μm, which was close to the original design (10 μm). This suggests that the DSLC method controlled the thickness of the SCs well using such a differential method [25]. Figure 2c reveals the X-ray diffraction (XRD) pattern

of the asymmetric SCs. We observed two sharp peaks at 19.9° and 40.4°, and they could be assigned as the (200) and (400) planes, respectively [31,32]. For polycrystalline films, more diffraction peaks were usually observed. Moreover, the full width at half maximum (FWHM) of the two diffraction peaks was only 0.17°. These results supported that the asymmetric micro-plates were single-crystalline and that the crystal growth occurred along the [100] direction [24].

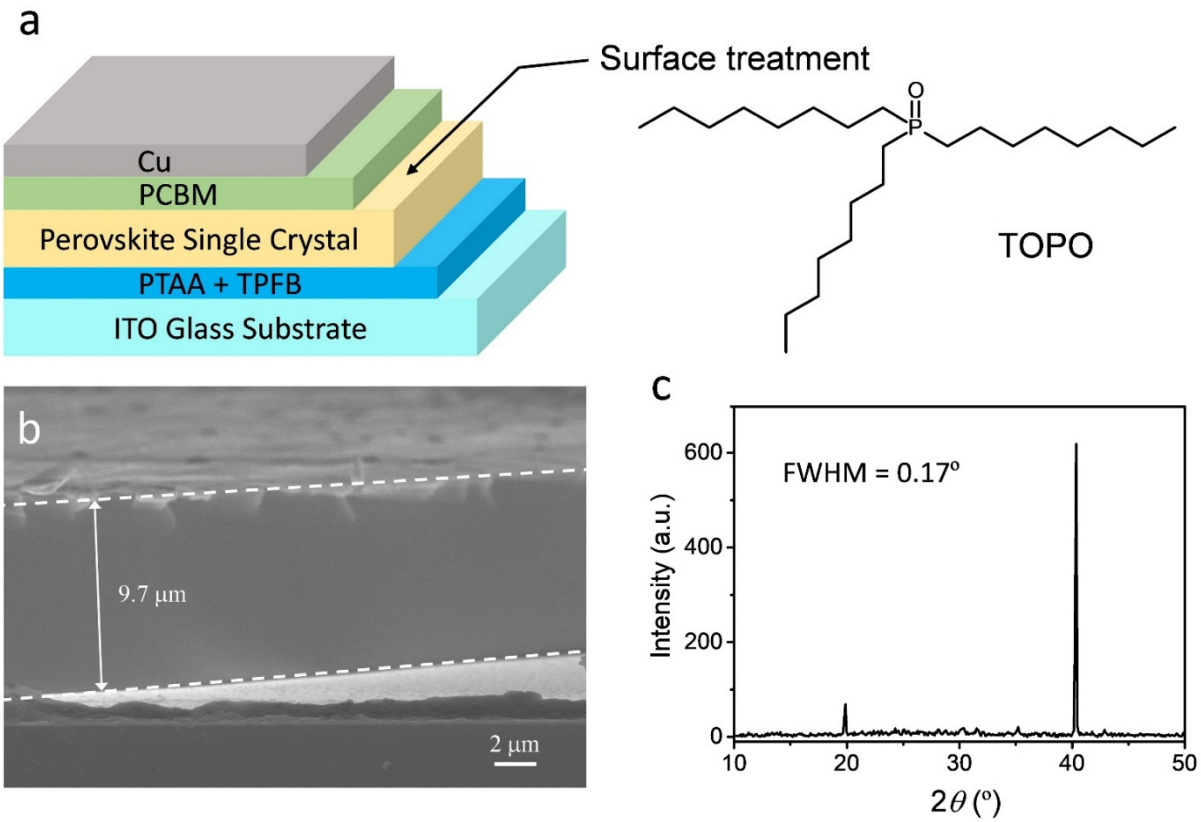

Figure 2. (**a**) The device structure of the single-crystal PeSCs in this work; (**b**) cross-sectional SEM image of the SCs; the thickness of the SC was approximately 10 μm; (**c**) XRD spectrum of the perovskite single crystal micro-plate.

Although the defect densities in perovskite SCs are lower than conventional polycrystalline thin films, surface defects are still very common because of the presence of uncoordinated atoms, missing atoms/molecules, and/or structure imperfections [33–35]. The surface imperfections could mainly contribute to the total defect density of PeSCs and significantly affect the device performance. To passivate the surface defects, TOPO solutions prepared with various concentrations were spin-coated on the as-prepared SCs (Figure 1). As shown in Figure 2a, TOPO is a Lewis base and is expected to behave as monodentate ligands to passivate the surface defects [36–38]. The concentrations of the TOPO solutions were 1.5, 1.8, 2.0, 2.3, and 2.5 mg mL^{-1}; hereafter, we denote these samples treated with various TOPO solutions as TOPO1.5, TOPO1.8. TOPO2.0, TOPO2.3, and TOPO2.5, respectively.

To investigate the passivation effects of TOPO, we examined the photoluminescence (PL) behavior of the passivated SCs prepared with various concentrations of TOPO; the steady-state PL spectra are displayed in Figure 3a. The peak position of the emission from the SC prepared without any treatment is located at 785 nm. The emission peak slightly red-shifted with the increasing TOPO concentration and it shifted to 792 nm for the TOPO2.0 sample. In fact, a similar red-shift of the PL peaks upon the surface passivation has been reported previously [36,37]. We suspect that the composition at the surface layers was probably altered slightly. Further, the PL intensity also increased with the increasing

TOPO concentration, suggesting that some defects affecting the radiation recombination of the excitons were passivated. When the concentration of the TOPO solution was further increased to 2.3 and 2.5 mg mL^{-1}, the peak started to shift toward shorter wavelengths. The peak positions were 786 and 780 nm for the TOPO2.3 and TOPO2.5 samples, respectively. The slightly blue-shifted PL peak implied a lower trap density near the band-edge of the passivated perovskite thin films [39,40]. Moreover, the PL intensity was also increased with the TOPO concentration up to 2.0 mg ml^{-1}; it decreased when the concentration was either 2.3 or 2.5 mg mL^{-1}. The above results indicated that the TOPO treatment could mitigate the surface defects of the SCs effectively.

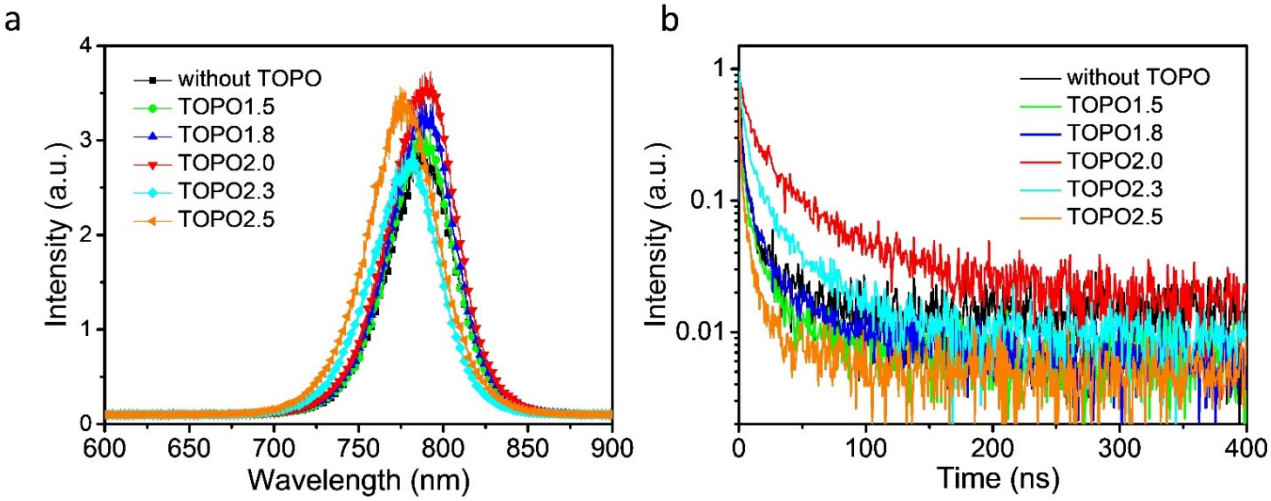

Figure 3. (**a**) Normalized steady-state and (**b**) time-resolved PL spectra of the perovskite SCs prepared with various concentrations of TOPO.

The optical properties were also studied using time-resolved photoluminescent (TRPL) spectroscopy; the results are revealed in Figure 3b. The TRPL decay curves of the SCs passivated with different TOPO concentrations were best fitted to the following bi-exponential decay equation [41,42]:

$$f(t) = A_1 e^{-t/\tau_1} + A_2 e^{-t/\tau_2} \quad (1)$$

where the per-factors, A_1 and A_2, were the amplitudes of the profiles; τ_2 and τ_1 were the first and second exponential constants, respectively. Basically, τ_1 is usually assigned to surface recombination and τ_2 is attributed to radiative recombination [42]. The fitting results are further summarized in Table 1. The lifetimes, τ_1 and τ_2, were 1.57 and 13.24 ns, respectively, resulting in an average lifetime (τ_{avg}) of 8.03 ns. They increased upon increasing the TOPO concentrations in the beginning of the treatment. When the concentration was 2.0 mg mL^{-1}, we observed the longest lifetimes, τ_1 and τ_2, of 8.66 and 55.10 ns, respectively, suggesting that a lower degree of defect density was achieved. Similar to the results of steady-state PL, the lifetimes decreased again if the TOPO concentration was further increased to 2.3 or 2.5 mg mL^{-1}. We suspect that the crystallinity of the perovskite SCs changed once the TOPO concentrations were higher than 2.0 mg mL^{-1}, leading to shorter PL lifetimes.

PeSCs were fabricated using the as-prepared perovskite single-crystal micro-plates. Figure 4a displays the *J*–*V* curves of the single-crystal PeSCs treated with various concentrations of TOPO solutions under the standard solar illumination condition (100 mW cm^{-2}, AM1.5G). The cell prepared without any treatment exhibited a typical photovoltaic performance, with an open-circuit voltage (V_{oc}) of 0.89 V, a short-circuit current density (J_{sc}) of 24.85 mA cm^{-2}, and a fill factor (*FF*) of 0.55, resulting in a PCE of 12.20%. After the treatment of TOPO solutions, the device performance was apparently improved. For instance, under the optimized condition, where the TOPO concentration was 2.0 mg ml^{-1}, the values of V_{oc}, J_{sc}, and *FF* increased to 1.02 V, 26.10 mA cm^{-2}, and 0.58, respectively, resulting in a best PCE of 15.65%. Table 2 summarizes the electrical properties of the

single-crystal PeSCs treated with various concentrations of TOPO. On average, the PCE was improved from 11.90 ± 0.30% to 14.76 ± 0.65% after TOPO treatments. The increase of 24% in PCE values suggests that the TOPO treatment is an effective method for improving the performance of single-crystal PeSCs. We also calculated the series (R_s) and shunt (R_{sh}) resistances for the PeSCs prepared under different conditions (Table 3). The R_s values decreased monotonically with the increasing TOPO concentration, revealing that TOPO could indeed passivate the traps/defects effectively. On the other hand, the R_{sh} values increased firstly but decreased upon the TOPO concentration exceeding 2.0 mg mL^{-1}, thereby affecting the device efficiencies. The above results support our previous suspicion that the crystallinity/molecule arrangements were affected at high TOPO concentrations (TOPO2.3 and TOPO2.5).

Table 1. Lifetime parameters of perovskite single crystals prepared with TOPO treatments at various concentrations.

Concentration of TOPO (mg mL^{-1})	τ_1 (ns)	τ_2 (ns)	τ_{avg} (ns)
0	1.57	13.24	8.03
1.5	2.48	19.44	12.74
1.8	4.02	29.33	18.91
2.0	8.66	55.10	40.96
2.3	4.75	30.66	21.06
2.5	2.78	17.82	11.56

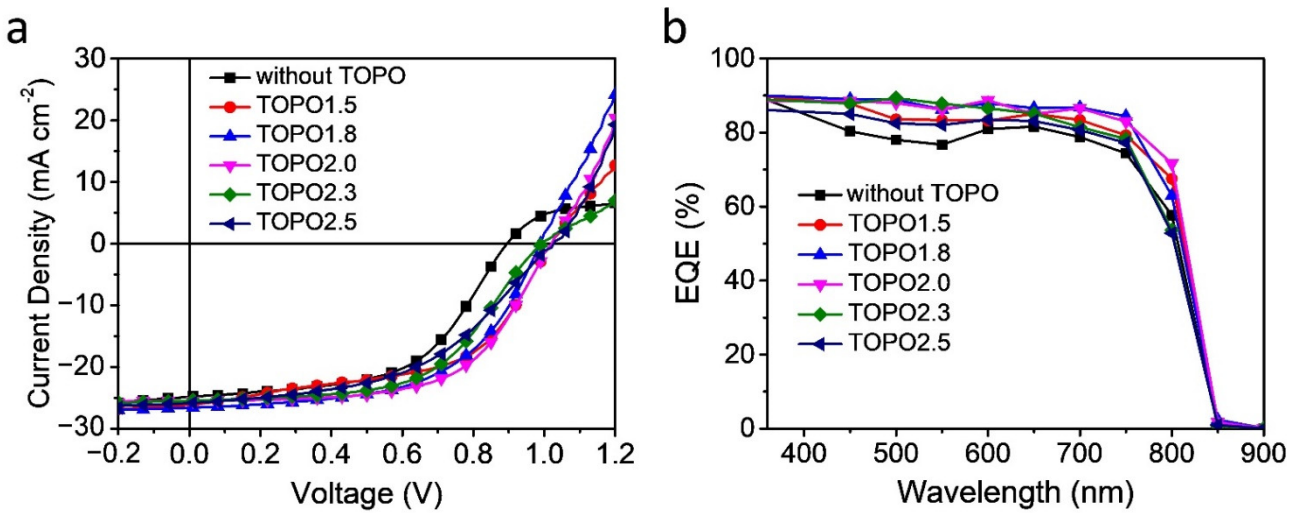

Figure 4. Electrical properties of the single-crystal PeSCs. (**a**) *J*–*V* curves of the PeSCs prepared with various concentrations of TOPO; the devices were measured under standard-condition illumination (100 mW cm^{-2}, AM1.5G). (**b**) Corresponding EQE spectra of the single-crystal PeSCs.

Table 2. Electrical characteristics of perovskite single-crystal solar cells prepared with various TOPO concentrations.

Concentration of TOPO (mg mL^{-1})	V_{oc} (V)	J_{sc} (mA cm^{-2})	*FF*	*PCE* (%)
0	0.89 ± 0.01	25.00 ± 0.23	0.50 ± 0.02	11.90 ± 0.30
1.5	0.99 ± 0.04	25.26 ± 0.72	0.53 ± 0.01	13.13 ± 0.60
1.8	0.99 ± 0.02	26.25 ± 0.35	0.56 ± 0.01	14.03 ± 0.70
2.0	0.99 ± 0.05	26.36 ± 0.48	0.59 ± 0.01	14.76 ± 0.65
2.3	1.00 ± 0.03	26.52 ± 0.28	0.53 ± 0.02	13.77 ± 0.40
2.5	1.03 ± 0.02	26.73 ± 0.45	0.53 ± 0.02	13.33 ± 0.45

Table 3. Series (R_S) and shunt (R_{SH}) resistances of the single-crystal PeSCs in this study.

Concentration of TOPO (mg mL^{-1})	0	1.5	1.8	2.0	2.3	2.5
R_S (Ω cm^2)	17.54	12.21	10.40	10.43	10.10	7.89
R_{SH} (Ω cm^2)	251.23	362.94	481.24	864.14	449.28	348.89

Figure 4b shows the external quantum efficiency (EQE) spectra of the various PeSCs. We can see that the shape of the spectrum did not change too much after the passivation using TOPO solutions. Integrating the EQE spectra of the single-crystal PeSCs treated with 0, 1.5, 1.8, 2.0, 2.3, and 2.5 mg mL^{-1} TOPO solutions provided photocurrents of 23.46, 25.14, 25.90, 26.02, 25.00, and 24.15 mA cm^{-2}, respectively. The results were very close to the photocurrent values that we obtained from the *J*–*V* curves directly under one-sun illumination (Figure 3a), and similar trends in the photocurrent values further supported the conclusion we drew from the *J*–*V* curves.

We also fabricated hole-only devices from the single-crystal micro-plates to study the passivation effect on the trap density. The device structure was ITO/PTAA/single crystal /MoO_3 (10 nm)/Cu, where MoO_3 served as the hole injection layer. The *J*–*V* curves of the devices prepared without treatment and treated with the 2.0 mg mL^{-1} TOPO solution were measured in the dark and the results are displayed in Figure 5a, respectively. Typical *J*–*V* characteristic shows three regions, namely, linear ohmic response at low bias voltage, nonlinear trap-filling region, and the region of the space-charge-limited current (SCLC) [14]. From the nonlinear trap-filling region, the trap-filled limit voltage (V_{TFL}) can be related to the trap density (n_t) according to Equation (2) [14,24]:

$$V_{TFL} = (en_tL^2)/(2\varepsilon\varepsilon_0) \quad (2)$$

where e is the elementary charge (1.6×10^{-19} C), L is the film thickness, ε is the dielectric constant, and ε_0 is the vacuum permittivity [14,24]. The resulting V_{TFL} values were 0.62 and 0.55 V for the devices prepared without and with TOPO solutions, respectively. The calculated trap density of the SC prepared without treatment was 2.2×10^{13} cm^{-3}; the order of the trap density was consistence with our previous works [24]. We noted that the typical n_t value was larger than 10^{16} cm^{-3} for polycrystalline devices [43], and the much lower n_t value we obtained herein supported the single-crystal nature of the perovskite micro-plates. Further, the trap density of the SC prepared with TOPO decreased to 1.9×10^{13} cm^{-3}, further confirming that the traps had been filled by the TOPO treatment.

PeSCs generally exhibit hysteresis behavior, which exhibits delayed *J*–*V* characteristics. Hysteresis in PeSCs is possibly related to ion migration, ferroelectric behavior, and the trapping/detrapping of carriers in the active layers [44]. In principle, the hysteresis is also affected by the imperfection of the active layers in PeSCs. The electrical curves of the single-crystal PeSCs were measured in both opposite directions (Figure 5b). We observed hysteresis behavior in the *J*–*V* characteristics for all of the devices that we fabricated in this work. To investigate the hysteresis quantitatively, we adopted an adimensional hysteresis index (HI), which, according to the definition reported previously, reveals the difference in power output with respect to the scan directions [45]. The calculated HI for the device prepared without TOPO treatment was 0.067, and the value was reduced to 0.042 after TOPO treatment. Therefore, we deduced that the reduced defects inhibited the degree of hysteresis behavior.

The passivated effects on the stability of the single-crystal PeSCs were also evaluated. Figure 6 displays the normalized time-dependent PCEs of the single-crystal PeSCs prepared with and without TOPO treatments. In the first 4 days during the stability test, the two PeSCs exhibited a comparable stability; the efficiencies of the device prepared without TOPO treatments was even slightly higher after normalization. After 4 days, however, the performance of the device prepared without TOPO treatments decayed significantly. The PCE of the device prepared with TOPO treatments only decreased slightly, and maintained

more than 76% of the original value even after 9 days. As shown in Figure 1, TOPO is hydrophobic due to its the long alkyl chains. The TOPO molecules on the surface of the SCs are beneficial for the humidity stability of the PeSCs.

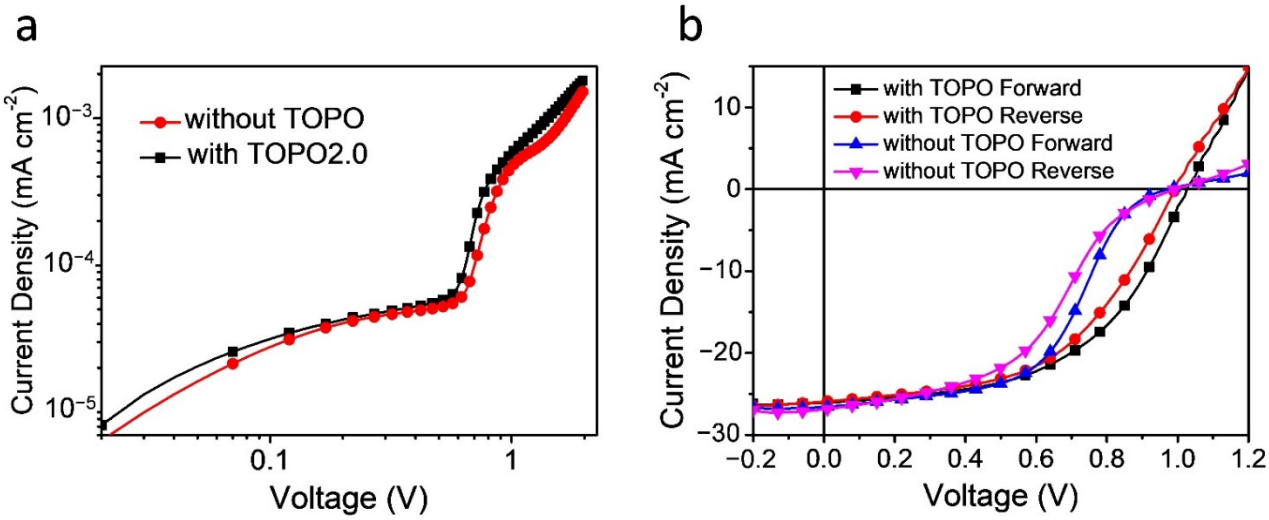

Figure 5. (**a**) *J*–*V* curves of hole-only devices prepared with and without TOPO treatment, measured in the dark; (**b**) *J*–*V* curves of single-crystal PeSCs, measured under standard one-sun illumination (100 mW cm^{-2}, AM1.5G) with two different scan directions. The TOPO concentration for treatment was 2.0 mg mL^{-1}.

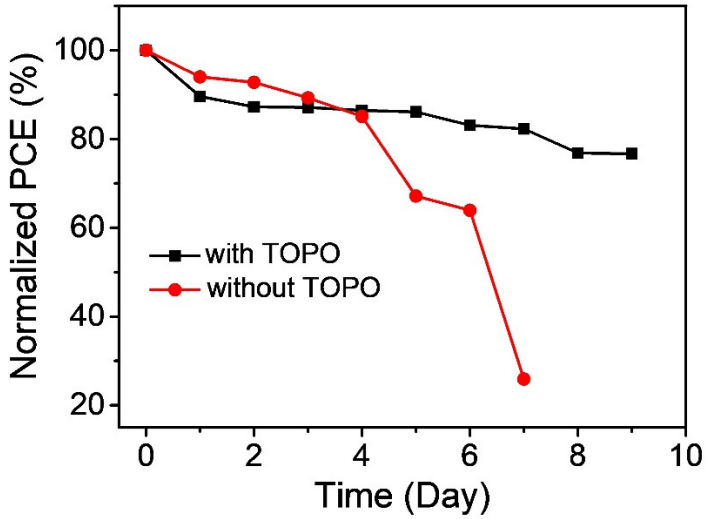

Figure 6. Normalized time-dependent PCEs of single-crystal PeSCs prepared with and without TOPO treatment. Both devices were stored in the dark at room temperature; the humidity of the stored environment was maintained at approximately 50 ± 10%. The TOPO concentration for treatment was 2.0 mg mL^{-1}.

4. Conclusions

In conclusion, the TOPO treatment is an effective passivation approach for improving the performance of single-crystal PeSCs. The PCE values, on average, can be improved by up to 24% under the optimized treatment condition. Under the optimal fabrication condition, the PCE is improved to 15.65%. The steady-state PL and TRPL results reveal that the surface defects can be effectively passivated, thereby prolonging the lifetimes of the PL emission from the SCs. The hole-only devices confirm that the defect density decreases after the TOPO treatment. The lower defect density of the treated device also inhibits the hysteresis behavior. Further, the TOPO treatment improves the stability of the single-crystal

PeSCs, presumably due to the hydrophobic long alkyl chains of the TOPO molecules. When perovskite SCs have considerably lower defects than their polycrystalline counterparts, the results in this work indicate that the surface defects still affect the device efficiencies significantly and that surface passivation is critical for achieving a high performance for single-crystal PeSCs.

Author Contributions: Conceptualization, T.-H.W. and F.-C.C.; methodology, F.-C.C.; formal analysis, T.-H.W. and F.-C.C.; resources, F.-C.C. and G.D.S.; data curation, T.-H.W.; writing—original draft preparation, T.-H.W. and F.-C.C.; writing—review and editing, F.-C.C. and G.D.S.; supervision, F.-C.C.; project administration, F.-C.C. and G.D.S.; funding acquisition, F.-C.C. and G.D.S. All authors have read and agreed to the published version of the manuscript.

Funding: This research was funded by the Ministry of Science and Technology of Taiwan, grant numbers MOST 109-2221-E-009-144-MY2 and MOST 109-2221-E-009-147-MY3 and the Ministry of Education (MOE) of Taiwan (SPROUT Project-Center for Emergent Functional Matter Science of National Yang Ming Chiao Tung University). The APC was funded by the Ministry of Science and Technology of Taiwan.

Institutional Review Board Statement: Not applicable.

Informed Consent Statement: Not applicable.

Data Availability Statement: Data are contained within the article.

Acknowledgments: This work was supported by the Ministry of Science and Technology of Taiwan and the Ministry of Education (MOE) of Taiwan (SPROUT Project-Center for Emergent Functional Matter Science of National Yang Ming Chiao Tung University).

Conflicts of Interest: The authors declare no conflict of interest.

References

1. Jena, A.K.; Kulkarni, A.; Miyasaka, T. Halide perovskite photovoltaics: Background, status, and future prospects. *Chem. Rev.* **2019**, *119*, 3036–3103. [CrossRef]
2. Wu, M.J.; Kuo, C.C.; Jhuang, L.S.; Chen, P.H.; Lai, Y.F.; Chen, F.C. Bandgap engineering enhances the performance of mixed-cation perovskite materials for indoor photovoltaic applications. *Adv. Energy Mater.* **2019**, *9*, 1901863. [CrossRef]
3. Zhang, C.; Kuang, D.B.; Wu, W.Q. A review of diverse halide perovskite morphologies for efficient optoelectronic applications. *Small Methods* **2020**, *4*, 1900662. [CrossRef]
4. Research Cell Record Efficiency Chart. Available online: https://www.nrel.gov/pv/assets/pdfs/best-research-cell-efficiencies-rev220126.pdf (accessed on 15 May 2022).
5. Gu, L.; Wen, K.; Peng, Q.; Huang, W.; Wang, J. Surface-plasmon-enhanced perovskite light-emitting diodes. *Small* **2020**, *16*, 2001861. [CrossRef]
6. Wang, Q.; Wang, X.; Yang, Z.; Zhou, N.; Deng, Y.; Zhao, J.; Xiao, X.; Rudd, P.; Moran, A.; Yan, Y.; et al. Efficient sky-blue perovskite light-emitting diodes via photoluminescence enhancement. *Nat. Commun.* **2019**, *10*, 5633. [CrossRef] [PubMed]
7. Jhuang, L.S.; Kumar, G.; Chen, F.C. Localized surface plasmon resonance of copper nanoparticles improves the performance of quasi-two-dimensional perovskite light-emitting diodes. *Dyes Pigm.* **2021**, *188*, 109204. [CrossRef]
8. Zhang, N.; Fan, Y.; Wang, K.; Gu, Z.; Wang, Y.; Ge, L.; Xiao, S.; Song, Q. All-optical control of lead halide perovskite microlasers. *Nat. Commun.* **2019**, *10*, 1770. [CrossRef] [PubMed]
9. Kao, T.S.; Hong, K.B.; Chou, Y.H.; Huang, J.F.; Chen, F.C.; Lu, T.C. Localized surface plasmon for enhanced lasing performance in solution-processed perovskites. *Opt. Express* **2016**, *24*, 20696–20702. [CrossRef]
10. Liu, D.; Yu, B.B.; Liao, M.; Jin, Z.; Zhou, L.; Zhang, X.; Wang, F.; He, H.; Gatti, T.; He, Z. Self-powered and broadband lead-free inorganic perovskite photodetector with high stability. *ACS Appl. Mater. Interfaces* **2020**, *12*, 30530–30537. [CrossRef]
11. Miao, J.; Zhang, F. Recent progress on highly sensitive perovskite photodetectors. *J. Mater. Chem. C* **2019**, *7*, 1741–1791. [CrossRef]
12. Wei, H.; Huang, J. Halide lead perovskites for ionizing radiation detection. *Nat. Commun.* **2019**, *10*, 1066. [CrossRef]
13. Zhou, Y.; Chen, J.; Bakr, O.M.; Omar, F.M. Metal halide perovskites for X-ray imaging scintillators and detectors. *ACS Energy Lett.* **2021**, *6*, 739–768. [CrossRef]
14. Dong, Q.; Fang, Y.; Shao, Y.; Mulligan, P.; Qiu, J.; Cao, L.; Huang, J. Electron-hole diffusion lengths > 175 μm in solution-grown $CH_3NH_3PbI_3$ single crystals. *Science* **2015**, *347*, 967–970. [CrossRef] [PubMed]
15. Wang, K.; Yang, D.; Wu, C.; Shapter, J.; Priya, S. Mono-crystalline perovskite photovoltaics toward ultrahigh efficiency? *Joule* **2019**, *3*, 311–316. [CrossRef]

16. Alsalloum, A.Y.; Turedi, B.; Zheng, X.; Mitra, S.; Zhumekenov, A.A.; Lee, K.J.; Maity, P.; Gereige, I.; AlSaggaf, A.; Roqan, I.S.; et al. Low-temperature crystallization enables 21.9% efficient single-crystal $MAPbI_3$ inverted perovskite solar cells. *ACS Energy Lett.* **2020**, *5*, 657–662. [CrossRef]
17. Chen, Z.; Dong, Q.; Liu, Y.; Bao, C.; Fang, Y.; Lin, Y.; Tang, S.; Wang, Q.; Xiao, X.; Bai, Y.; et al. Thin single crystal perovskite solar cells to harvest below-bandgap light absorption. *Nat. Commun.* **2017**, *8*, 1890. [CrossRef]
18. Peng, W.; Wang, L.; Murali, B.; Ho, K.T.; Bera, A.; Cho, N.; Kang, C.F.; Burlakov, V.M.; Pan, J.; Sinatra, L.; et al. Solution-grown monocrystalline hybrid perovskite films for hole-transporter-free solar cells. *Adv. Mater.* **2016**, *28*, 3383–3390. [CrossRef]
19. Alsalloum, A.Y.; Turedi, B.; Almasabi, K.; Zheng, X.; Naphade, R.; Stranks, S.D.; Mohammed, O.F.; Bakr, O.M. 22.8%-Efficient single-crystal mixed-cation inverted perovskite solar cells with a near-optimal bandgap. *Energy Environ. Sci.* **2021**, *14*, 2263–2268. [CrossRef]
20. Rao, H.S.; Li, W.G.; Chen, B.X.; Kuang, D.B.; Su, C.Y. In situ growth of 120 cm^2 $CH_3NH_3PbBr_3$ perovskite crystal film on FTO glass for narrowband-photodetectors. *Adv. Mater.* **2017**, *29*, 1602639. [CrossRef]
21. Lee, L.; Baek, J.; Park, K.S.; Lee, Y.E.; Shrestha, N.K.; Sung, M.M. Wafer-scale single-crystal perovskite patterned thin films based on geometrically-confined lateral crystal growth. *Nat. Commun.* **2017**, *8*, 15882. [CrossRef]
22. Huang, Y.; Zhang, Y.; Sun, J.; Wang, X.; Sun, J.; Chen, Q.; Pan, C.; Zhou, H. The exploration of carrier behavior in the inverted mixed perovskite single-crystal solar cells. *Adv. Mater. Interfaces* **2018**, *5*, 1800224. [CrossRef]
23. Yue, H.L.; Sung, H.H.; Chen, F.C. Seeded space-limited crystallization of $CH_3NH_3PbI_3$ single-crystal plates for perovskite solar cells. *Adv. Electron. Mater.* **2018**, *4*, 1700655. [CrossRef]
24. Kuo, C.C.; Sharma, D.G.; Chen, F.C. *p*-Doping the interfacial layers with tetrakis(pentafluorophenyl)borate improves the power conversion efficiencies in single-crystal perovskite solar cells. *Surf. Interfaces* **2022**, *30*, 101858. [CrossRef]
25. Sung, H.H.; Kuo, C.C.; Chiang, H.S.; Yue, H.L.; Chen, F.C. Differential space-limited crystallization of mixed-cation lead iodide single-crystal micro-plates enhances the performance of perovskite solar cells. *Solar RRL* **2019**, *3*, 1900130. [CrossRef]
26. Tsai, H.Y.; Yang, Y.F.; Jiang, H.S.; Chen, F.C. Asymmetrical single crystals containing tilted Ruddlesden–Popper phases for efficient perovskite solar cells. *Solar RRL* **2022**. [CrossRef]
27. Li, L.; Liu, J.; Zeng, M.; Fu, L. Space-confined growth of metal halide perovskite crystal films. *Nano Res.* **2021**, *14*, 1609–1624. [CrossRef]
28. Cheng, X.; Yang, S.; Cao, B.; Tao, X.; Chen, Z. Single crystal perovskite solar cells: Development and perspectives. *Adv. Funct. Mater.* **2020**, *30*, 1905021. [CrossRef]
29. Gao, W.; Zhang, Z.; Xu, R.; Chan, E.M.; Yuan, G.; Liu, J.M. Development and prospects of halide perovskite single crystal films. *Adv. Electron. Mater.* **2022**, *8*, 2100980. [CrossRef]
30. Huang, C.-F.; Keshtov, M.L.; Chen, F.C. Cross-linkable hole-transport materials improve the device performance of perovskite light-emitting diodes. *ACS Appl. Mater. Interfaces* **2016**, *8*, 27006–27011. [CrossRef]
31. Salado, M.; Calio, L.; Berger, R.; Kazim, S.; Ahmad, S. Influence of the mixed organic cation ratio in lead iodide based perovskite on the performance of solar cells. *Phys. Chem. Chem. Phys.* **2016**, *18*, 27148–27157. [CrossRef]
32. Lia, X.; Yang, J.; Jiang, Q.; Chu, W.; Zhang, D.; Zhou, Z.; Ren, Y.; Xin, J. Enhanced photovoltaic performance and stability in mixed-cation perovskite solar cells via compositional modulation. *Electrochim. Acta* **2017**, *247*, 460–467. [CrossRef]
33. Lei, Y.; Xu, Y.; Wang, M.; Zhu, G.; Jin, Z. Origin, influence, and countermeasures of defects in perovskite solar cells. *Small* **2021**, *17*, 2005495. [CrossRef] [PubMed]
34. Hsiao, M.C.; Chien, P.C.; Jhuang, L.S.; Chen, F.C. Bidentate chelating ligands as effective passivating materials for perovskite light-emitting diodes. *Phys. Chem. Chem. Phys.* **2019**, *21*, 7867–7873. [CrossRef]
35. Saykar, N.G.; Arya, A.; Mahapatra, S.K. A comprehensive review on defect passivation and gradient energy alignment strategies for highly efficient perovskite solar cells. *J. Phys. D Appl. Phys.* **2022**, *55*, 043001. [CrossRef]
36. deQuilettes, D.W.; Koch, S.; Burke, S.; Paranji, R.K.; Shropshire, A.J.; Ziffer, M.E.; Ginger, D.S. Photoluminescence lifetimes exceeding 8 µs and quantum yields exceeding 30% in hybrid perovskite thin films by ligand passivation. *ACS Energy Lett.* **2016**, *1*, 438–444. [CrossRef]
37. Li, W.; Lai, X.; Meng, F.; Li, G.; Wang, K.; Kyaw, A.K.K.; Sun, X.W. Efficient defect-passivation and charge-transfer with interfacial organophosphorus ligand modification for enhanced performance of perovskite solar cells. *Sol. Energy Mate. Sol. Cells* **2020**, *211*, 110527. [CrossRef]
38. Huang, G.; Wang, C.; Zhang, H.; Xu, S.; Xu, Q.; Cui, Y. Post-healing of defects: An alternative way for passivation of carbon-based mesoscopic perovskite solar cells via hydrophobic ligand coordination. *J. Mater. Chem. A* **2018**, *6*, 2449–2455. [CrossRef]
39. Afroz, M.A.; Garai, R.; Gupta, R.K.; Iyer, P.K. Additive-assisted defect passivation for minimization of open-circuit voltage loss and improved perovskite solar cell performance. *ACS Appl. Energy Mater.* **2021**, *4*, 10468–10476. [CrossRef]
40. Cao, Q.; Li, Y.; Zhang, H.; Yang, J.; Han, J.; Xu, T.; Wang, S.; Wang, Z.; Gao, B.; Zhao, J.; et al. Efficient and stable inverted perovskite solar cells with very high fill factors via incorporation of star-shaped polymer. *Sci. Adv.* **2021**, *7*, eabg06333. [CrossRef]
41. Zhumekenov, A.A.; Saidaminov, M.I.; Haque, M.A.; Alarousu, E.; Sarmah, S.P.; Murali, B.; Dursun, I.; Miao, X.H.; Abdelhady, A.L.; Wu, T.; et al. Formamidinium lead halide perovskite crystals with unprecedented long carrier dynamics and diffusion length. *ACS Energy Lett.* **2016**, *1*, 32–37. [CrossRef]
42. Song, T.B.; Chen, Q.; Zhou, H.; Luo, S.; Yang, Y.; You, J.; Yang, Y. Unraveling film transformations and device performance of planar perovskite solar cells. *Nano Energy* **2015**, *12*, 494–500. [CrossRef]

43. Yin, G.; Ma, J.; Jiang, H.; Li, J.; Yang, D.; Gao, F.; Zeng, J.; Liu, Z.; Liu, S.F. Enhancing efficiency and stability of perovskite solar cells through Nb-doping of TiO2 at low temperature. *ACS Appl. Mater. Interfaces* **2017**, *9*, 10752–10758. [CrossRef] [PubMed]
44. Chen, B.; Yang, M.; Priya, S.; Zhu, K. Origin of J–V hysteresis in perovskite solar cells. *J. Phys. Chem. Lett.* **2016**, *7*, 905–917. [CrossRef] [PubMed]
45. Lee, J.W.; Kim, S.G.; Bae, S.H.; Lee, D.K.; Lin, O.; Yang, Y.; Park, N.G. The interplay between trap density and hysteresis in planar heterojunction perovskite solar cells. *Nano Lett.* **2017**, *17*, 4270–4276. [CrossRef]